

# DAPS++: Rethinking Diffusion Inverse Problems with Decoupled Posterior Annealing

Hao Chen<sup>1</sup> Renzheng Zhang<sup>2</sup> Scott S. Howard<sup>1</sup>

<sup>1</sup>Department of Electrical Engineering, University of Notre Dame

<sup>2</sup>Department of Aerospace and Mechanical Engineering, University of Notre Dame

hchen27@nd.edu rzheng4@nd.edu showard@nd.edu

## Abstract

*From a Bayesian perspective, score-based diffusion solves inverse problems through joint inference, embedding the likelihood with the prior to guide the sampling process. However, this formulation fails to explain its practical behavior: the prior offers limited guidance, while reconstruction is largely driven by the measurement-consistency term, leading to an inference process that is effectively decoupled from the diffusion dynamics. To clarify this structure, we reinterpret the role of diffusion in inverse problem solving as an initialization stage within an expectation–maximization (EM)–style framework, where the diffusion stage and the data-driven refinement are fully decoupled. We introduce DAPS++, which allows the likelihood term to guide inference more directly while maintaining numerical stability and providing insight into why unified diffusion trajectories remain effective in practice. By requiring fewer function evaluations (NFEs) and measurement-optimization steps, DAPS++ achieves high computational efficiency and robust reconstruction performance across diverse image restoration tasks.*

## 1. Introduction

Solving ill-posed inverse problems is fundamental in science and engineering, particularly in scientific imaging—such as astrophotography [21, 23] and biomedical imaging [7, 10, 14, 22, 30]—with broad applications in real-world systems. These problems aim to reconstruct the original signal  $\mathbf{x}_0$  from observations  $\mathbf{y}$  acquired under various restoration or measurement conditions, assuming a known forward model [32]. A common strategy is to formulate the inverse problem within a Bayesian framework [5], where  $p(\mathbf{x}_0|\mathbf{y}) \propto p(\mathbf{y}|\mathbf{x}_0)p(\mathbf{x}_0)$ . Here, the likelihood  $p(\mathbf{y}|\mathbf{x}_0)$  characterizes the measurement process, while the prior  $p(\mathbf{x}_0)$  encodes structural assumptions about the underlying signal.

Classical Bayesian inverse problem formulations often rely on Tikhonov, total variation (TV), or wavelet-based priors to constrain the solution space and stabilize reconstruction [11, 31]. Modern generative models [13, 24, 26], particularly score-based diffusion methods [16, 27–29], provide far more expressive high-dimensional priors and have become widely adopted in Bayesian inverse problem frameworks [1, 4, 9, 38]. These methods incorporate measurement information into the sampling dynamics by injecting an approximate likelihood gradient  $\nabla_{\mathbf{x}_t} \log p(\mathbf{y}|\mathbf{x}_t)$  at each diffusion timestep. By solving stochastic differential equations (SDEs) or their deterministic ODE counterparts [19, 20], diffusion models transform an initial noise sample  $\mathbf{x}_T$  toward the data manifold  $\mathbf{x}_0$ , conditioned on the observation  $\mathbf{y}$ .

More recently, decoupled formulations such as DCDP [18] and DAPS [38] explicitly separate the diffusion prior  $p(\mathbf{x}_0)$  from the data-consistency term  $p(\mathbf{y}|\mathbf{x}_0)$  at the algorithmic level. In these methods, diffusion updates and measurement updates alternate: each data-consistency step moves the estimate toward the observation, and the subsequent re-noising step restores the appropriate annealed noise level. As the noise level decreases, the resulting time-marginal distribution  $\pi(\mathbf{x}_t|\mathbf{y})$  is assumed to approach the posterior  $p(\mathbf{x}_0|\mathbf{y})$ . Although implemented in a decoupled manner, the overall framework remains nominally Bayesian, since each marginal still depends on the prior gradient  $\nabla_{\mathbf{x}_t} \log p_t(\mathbf{x}_t)$ .

However, this expected trajectory rarely holds in practice. The data-consistency gradient often dominates the update dynamics, causing each intermediate distribution  $\pi(\mathbf{x}_t|\mathbf{y})$  to act as an isolated approximation of the posterior rather than part of a coherent sequence of marginals. As a result, the path from  $\mathbf{x}_T$  to  $\mathbf{x}_0$  becomes a set of loosely connected estimates rather than a consistent posterior evolution. This reveals that a strictly Bayesian interpretation is insufficient for explaining the empirical behavior of diffusion-based inverse problem solvers. Since diffusion updates and data-consistency updates effectively operate indepen-

dently, an expectation–maximization (EM)–style viewpoint becomes more suitable: the diffusion stage defines a flat prior space that constrains feasible solutions, while the likelihood gradient  $\nabla_{\mathbf{x}_0} \log p(\mathbf{y}|\mathbf{x}_0)$  is refined within this space through an Markov chain Monte Carlo (MCMC)–style update. The two stages are thus naturally decoupled, corresponding to prior initialization followed by likelihood–driven correction.

Building on this perspective, we refine the understanding of why diffusion-based inverse problem solvers are effective and introduce **DAPS++**. Leveraging the principles of Decoupled Annealing Posterior Sampling (DAPS), our method provides a more efficient and interpretable formulation of diffusion-based Bayesian inference using diffusion models that operate directly in pixel space. Empirically, **DAPS++** delivers strong performance across a broad set of inverse problems—including both linear and nonlinear image restoration while offering substantially faster sampling than existing approaches. Compared with DAPS and other diffusion-based inverse problem methods, **DAPS++** achieves comparable or superior reconstruction quality while reducing sampling time and neural function evaluations (NFEs) by approximately **90%** on both the FFHQ validation set and the ImageNet test dataset.

## 2. Related Work

### 2.1. Diffusion Models

Score-based diffusion models [13, 16, 27–29] learn the data distribution  $p(\mathbf{x}_0)$  and its gradient, generating samples by progressively denoising Gaussian-corrupted data. A sequence of isotropic Gaussian perturbations  $\mathcal{N}(0, \sigma_t^2 \mathbf{I})$  is applied to the data, inducing a family of noise-conditioned distributions  $p(\mathbf{x}; \sigma_t)$ . The model is trained to estimate the gradient of the log-density—i.e., the *score function*—across time steps  $t \in [0, T]$ , or equivalently across decreasing noise levels  $\sigma_t$  from  $\sigma_T = \sigma_{\max}$  to  $\sigma_0 = 0$ . When  $\sigma_{\max}$  is sufficiently large, the terminal distribution approaches pure Gaussian noise,  $\mathcal{N}(0, \sigma_{\max}^2 \mathbf{I})$ .

During sampling, the learned model approximates the true score of  $p_t(\mathbf{x}; \sigma_t)$  via  $s_\theta(\mathbf{x}, \sigma_t) \approx \nabla_{\mathbf{x}} \log p_t(\mathbf{x}; \sigma_t)$ . Starting from pure noise  $\mathbf{x}_T \sim \mathcal{N}(0, \sigma_{\max}^2 \mathbf{I})$ , the generative process follows the reverse stochastic differential equation (SDE)

$$d\mathbf{x}_t = -2 \dot{\sigma}_t \sigma_t \nabla_{\mathbf{x}_t} \log p_t(\mathbf{x}_t; \sigma_t) dt + \sqrt{2 \dot{\sigma}_t \sigma_t} d\mathbf{w}_t, \quad (1)$$

where  $\dot{\sigma}_t$  is the derivative of the noise schedule,  $d\mathbf{w}_t$  is a standard Wiener process, and the formulation follows the variance-exploding (VE) or EDM parameterization.

### 2.2. Inverse Problems with Diffusion Models

A general inverse problem seeks to recover the unknown signal  $\mathbf{x}_0$  from noisy measurements  $\mathbf{y}$ . Given a forward

operator  $\mathcal{A}$ , the measurement model is  $\mathbf{y} = \mathcal{A}(\mathbf{x}_0) + \mathbf{n}$ , where  $\mathbf{n}$  is additive Gaussian noise  $\mathcal{N}(0, \gamma^2 \mathbf{I})$ . Under a Bayesian formulation, the posterior satisfies  $p(\mathbf{x}_0|\mathbf{y}) \propto p(\mathbf{y}|\mathbf{x}_0)p(\mathbf{x}_0)$ , with the likelihood term  $p(\mathbf{y}|\mathbf{x}_0) = \mathcal{N}(\mathcal{A}(\mathbf{x}_0), \gamma^2 \mathbf{I})$ .

To incorporate the diffusion prior into inverse problems, a standard approach is to form a joint SDE by adding the data-consistency term to Eq. 1, giving

$$\begin{aligned} d\mathbf{x}_t = & -2 \dot{\sigma}_t \sigma_t \nabla_{\mathbf{x}_t} \log p_t(\mathbf{x}_t; \sigma_t) dt \\ & - 2 \dot{\sigma}_t \sigma_t \nabla_{\mathbf{x}_t} \log p_t(\mathbf{y} | \mathbf{x}_t; \sigma_t) dt \\ & + \sqrt{2 \dot{\sigma}_t \sigma_t} d\mathbf{w}_t \end{aligned} \quad (2)$$

which combines the diffusion prior drift with a measurement-consistency term.

In practice, measurement consistency is defined in terms of the clean likelihood  $p(\mathbf{y}|\mathbf{x}_0)$ ; as a result, the noised likelihood  $p(\mathbf{y}|\mathbf{x}_t; \sigma_t)$  is typically inaccessible or ill-defined. Several approaches approximate this quantity [2, 25, 36] to embed measurement guidance directly into the diffusion process. Among these, Diffusion Posterior Sampling (DPS) [4] employs Tweedie’s formula to estimate  $p(\mathbf{y}|\mathbf{x}_t) \approx p(\mathbf{y}|\mathbf{x}_0 = \mathbb{E}[\mathbf{x}_0|\mathbf{x}_t])$ , achieving strong empirical performance. However, recent studies show that DPS behaves more like a maximum a posteriori (MAP) estimator than a true posterior sampler [35, 37]. This has motivated data-consistency frameworks [18, 25] that incorporate explicit likelihood optimization into diffusion-based solvers. Nevertheless, approaches that minimize  $\nabla_{\mathbf{x}_t} \log p_t(\mathbf{y}|\mathbf{x}_t; \sigma_t)$  often exhibit instability due to overfitting. Another line of work uses SVD-based projections and projection-driven sampling [3, 17, 33] to enforce measurement constraints, while recent decoupled frameworks such as DAPS [38] reformulate Eq. 2 into a two-stage structure that preserves the time-marginal distribution.

However, similarly to DPS, such decoupled methods deviate from posterior sampling as defined in Eq. 2, because they implicitly assume that the time-marginal distributions remain consistent with the true posterior given  $\hat{\mathbf{x}}_0(\mathbf{x}_t)$ —an assumption that does not hold in practice. In reality, the two stages function as separate generation and optimization procedures rather than components of a unified posterior sampler, limiting both the theoretical validity and computational efficiency of the framework. This motivates reinterpreting diffusion-based inverse problem solvers primarily as methods for optimizing  $p(\mathbf{y}|\mathbf{x}_0)$  within a diffusion-generated solution space, providing a more accurate perspective for diffusion-based inference.

## 3. Method

### 3.1. Breakdown of Prior Guidance

**Motivation.** We begin by analyzing the interaction between the prior and likelihood gradients to clarify when and why

diffusion priors contribute only marginally to reconstruction. This observation motivates the stage-separation design used in the proposed framework.

To quantify the directional relationship between the prior and likelihood terms, we examine the empirical inner product

$$A_t = \left\langle \nabla_{\mathbf{x}_t} \log p_t(\mathbf{y} | \mathbf{x}_t; \sigma_t), \nabla_{\mathbf{x}_t} \log p_t(\mathbf{x}_t; \sigma_t) \right\rangle, \quad (3)$$

where  $\nabla_{\mathbf{x}_t} \log p_t(\mathbf{y} | \mathbf{x}_t; \sigma_t)$  and  $\nabla_{\mathbf{x}_t} \log p_t(\mathbf{x}_t; \sigma_t)$  denote the likelihood and prior gradients at noise level  $\sigma_t$ , respectively. Under high-noise conditions, the expected value of this inner product is close to zero, implying that the two gradients are effectively uncorrelated. This orthogonality helps explain why methods such as DPS can combine these terms without destructive interference (see Section 3.4).

To assess the relative strength of the two components, we define the gradient ratio

$$\kappa_t := \frac{\|\nabla_{\mathbf{x}_t} \log p_t(\mathbf{y} | \mathbf{x}_t; \sigma_t)\|}{\|\nabla_{\mathbf{x}_t} \log p_t(\mathbf{x}_t; \sigma_t)\|}. \quad (4)$$

where  $\kappa_t$  measures the dominance of the data-consistency gradient relative to the prior gradient. Under the Gaussian noise model  $p(\mathbf{y} | \mathbf{x}_0) = \mathcal{N}(\mathcal{A}(\mathbf{x}_0), \gamma^2 \mathbf{I})$ , the likelihood term at noise level  $\sigma_t$  may be approximated by

$$\nabla_{\mathbf{x}_t} \log p_t(\mathbf{y} | \mathbf{x}_t; \sigma_t) \simeq -\frac{1}{\gamma^2} \nabla_{\mathbf{x}_t} \|\mathbf{y} - \mathcal{A}(\hat{\mathbf{x}}_0(\mathbf{x}_t))\|^2 \quad (5)$$

where  $\mathcal{A}(\cdot)$  is the measurement operator and  $\hat{\mathbf{x}}_0(\mathbf{x}_t)$  denotes the denoised estimate associated with state  $\mathbf{x}_t$ .

Together with the criterion  $\kappa_t \gg 1$ , as shown in Fig. 1(a), the analysis indicates that the diffusion prior provides only a negligible contribution to the optimization, supporting its removal in the DAPS++ framework. A corresponding  $L$ -Lipschitz argument in the Appendix further shows that the prior gradient  $\nabla_{\mathbf{x}_t} \log p_t(\mathbf{x}_t; \sigma_t)$  within the time-marginal formulation makes only a limited impact on the update. In practice, reconstruction is driven almost entirely by the data-consistency term, and as confirmed in Fig. 1(b), omitting the prior component in the time-marginal yields nearly identical reconstruction quality, validating its minimal influence.

### 3.2. Complete Stage Separation via EM Reformulation

Under this observation, decoupled noise-annealing approaches do not strictly follow the time-marginal distribution, especially when initialized from high-noise conditions. Nevertheless, they perform well empirically, as the diffusion model still produces high-quality reconstructions from the measurements. To explain this behavior, we reinterpret the process as two fully independent stages inspired by an expectation–maximization (EM) viewpoint, yielding a

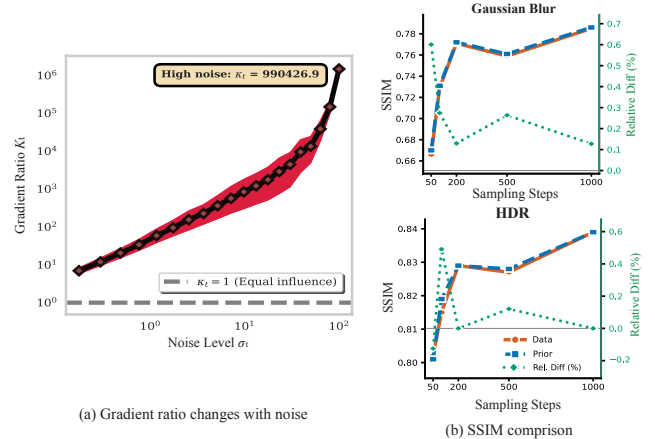


Figure 1. (a) Evolution of the gradient ratio  $\kappa_t$  with respect to noise level and its relative error during a Gaussian-blur iteration, illustrating that the data-consistency gradient dominates throughout the optimization process. (b) Comparison between DAPS results using the **prior** term and using only the **data** term across different numbers of annealing steps, showing that the prior contributes minimally and mainly shapes the time-marginal distribution.

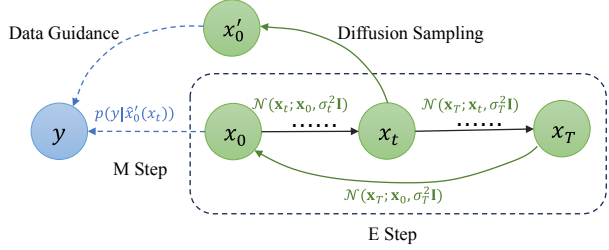


Figure 2. Diagram of the **DAPS++** framework. The E-step provides the initial state and constructs the constrained optimization space  $p(\mathbf{x}_0)$  for data-driven MCMC refinement, while the M-step optimizes within this space under measurement guidance. The two steps are fully decoupled, and after each M-step, controlled noise is re-injected by the diffusion process to initiate the next E-step.

complete separation between diffusion-based initialization and posterior refinement, as illustrated in Fig. 2.

**Expectation step.** Solving the diffusion SDE produces samples consistent with the learned prior  $p(\mathbf{x}_0)$ , providing an initialization whose mean and variance are close to the target distribution. Because high-noise initialization randomizes the state far from the data manifold, using higher-order solvers or more diffusion steps in DAPS typically does not further improve pixel-domain initialization. Tweedie’s formula offers a principled estimator of the conditional mean:

$$\mathbb{E}[\mathbf{x}_0 | \mathbf{x}_t] \approx \mathbf{x}_t + \sigma_t^2 s_\theta(\mathbf{x}_t, \sigma_t), \quad (6)$$

where  $s_\theta(\mathbf{x}_t, \sigma_t)$  denotes the learned score function. To balance efficiency and fidelity, DAPS++ introduces a noise

threshold  $\bar{\sigma}$ : for  $\sigma_t > \bar{\sigma}$ , Tweedie denoising (Eq. 6) yields fast initialization; for  $\sigma_t \leq \bar{\sigma}$ , a single higher-order ODE step is used to preserve fine details at minimal cost.

**Maximization step.** This step refines the estimate by performing a likelihood–driven update to enforce measurement consistency within the diffusion–constrained domain. Since the diffusion model initializes samples close to the high–density region of  $p(\mathbf{x}_0)$  (See Appendix about manifold–proximity analysis), the search space is already aligned with the target posterior, allowing Markov chain Monte Carlo (MCMC) to converge with substantially fewer iterations. Following the unadjusted Langevin algorithm (ULA), the update rule is

$$\begin{aligned} \mathbf{x}_0^{(j+1)} = \mathbf{x}_0^{(j)} &+ \eta \left( \nabla_{\mathbf{x}_0^{(j)}} \log p(\mathbf{y} \mid \mathbf{x}_0^{(j)}) \right. \\ &\left. + \nabla_{\mathbf{x}_0^{(j)}} \log p(\mathbf{x}_0^{(j)}) \right) + \sqrt{2\eta} \boldsymbol{\epsilon}_j, \end{aligned} \quad (7)$$

where  $\eta$  is the step size and  $\boldsymbol{\epsilon}_j \sim \mathcal{N}(\mathbf{0}, \mathbf{I})$  denotes Gaussian perturbation for stochastic exploration.

In standard MCMC, the prior gradient term  $\nabla_{\mathbf{x}_0^{(j)}} \log p(\mathbf{x}_0^{(j)})$  serves as a regularization component. However, because diffusion initialization places  $\mathbf{x}_0^{(j)}$  in a region where the score magnitude satisfies  $\|\nabla \log p(\mathbf{x}_0)\| = O(\varepsilon)$ , this contribution becomes numerically negligible. We therefore omit it and obtain a likelihood–driven refinement step that remains stable and computationally efficient, since only a few informed updates are required within the restricted domain.

Although this refinement drives the estimate toward the clean target, it reduces variability associated with noise–corrupted or unobserved components. To restore this variability, each M–step is followed by a re–noising stage that returns to the E–step, reintroducing structured uncertainty according to

$$\mathcal{Q}_t = \mathbb{E}_{\mathbf{x}_t \sim p_t(\mathbf{x}_t)} \left[ \log p(\mathbf{x}_0, \mathbf{x}_t \mid \mathbf{y}) \right], \quad (8)$$

which preserves the statistical characteristics of the diffusion prior while maintaining consistency with the measurement constraints.

Unlike a maximum a posteriori (MAP) approach that seeks a single optimum  $\arg \max_{\mathbf{x}_t} \log p_t(\mathbf{y} \mid \mathbf{x}_t; \sigma_t)$ , our method performs stochastic sampling within the diffusion–defined latent space, thereby exploring the posterior distribution rather than collapsing to one mode. To further improve convergence stability, we adopt an EDM-inspired annealing schedule in which the effective noise or step size decays polynomially (with exponent in the range  $[-4, -7]$ ), enabling smoother and more stable refinement under low–noise conditions.

### 3.3. DAPS++ for General Inverse Problems

The complete DAPS++ framework consists of two sequential stages that together form a fully decoupled pipeline.

**Stage 1: Diffusion-Based Initialization.** Starting from pure noise  $\mathbf{x}_T \sim \mathcal{N}(0, \sigma_{\max}^2 \mathbf{I})$ , we run the reverse diffusion process *without any likelihood guidance* to obtain  $\hat{\mathbf{x}}_0$  using Eq. 6 as noise scheduler smaller than  $\bar{\sigma}$ . This stage serves as a one-time initialization that approximates the manifold of the clean data distribution. The resulting  $\hat{\mathbf{x}}_0$  provides a sample within a flat prior space that captures the global structure of the signal and is passed directly to Stage 2 without invoking any additional prior information, ensuring complete decoupling between the two stages. Stage 2 only requires  $\hat{\mathbf{x}}_0 \in \mathcal{M}_{p(\mathbf{x}_0)}$ , since the subsequent MCMC refinement is independent of the specific initialization path.

**Stage 2: Likelihood-Driven MCMC Refinement.** Given the initialization  $\hat{\mathbf{x}}_0$ , we perform independent MCMC sampling driven solely by the likelihood term under the Gaussian measurement model. The update rule is

$$\mathbf{x}_0^{(j+1)} = \mathbf{x}_0^{(j)} - \frac{\eta}{\gamma^2} \nabla_{\mathbf{x}_0^{(j)}} \left\| \mathbf{y} - \mathcal{A}(\mathbf{x}_0^{(j)}) \right\|^2 + \sqrt{2\eta} \boldsymbol{\epsilon}_j \quad (9)$$

where  $\gamma$  controls the measurement noise level and  $\boldsymbol{\epsilon}_j \sim \mathcal{N}(\mathbf{0}, \mathbf{I})$  adds stochastic exploration. This refinement stage updates the sample strictly according to the measurement likelihood, allowing inference to be guided directly by the observation model while maintaining numerical stability.

While DAPS performs alternating E–M updates at every annealing diffusion timestep to preserve the time-marginal distribution, DAPS++ completes Stage 1 entirely before moving to Stage 2, thereby removing the need to balance prior and likelihood gradients during diffusion sampling. This full separation not only reduces the computational cost associated with repeated diffusion evaluations but also improves interpretability by isolating the generative prior (diffusion) from the data-consistency refinement (MCMC). A detailed algorithmic description and pseudocode are provided in the Appendix.

### 3.4. Connections to Existing Diffusion-Based Solvers

**Remark.** The E–M perspective introduced above also clarifies the behavior of existing diffusion-based solvers. Although many diffusion-based inverse problem approaches are presented as posterior samplers, recent studies show that their updates often resemble MAP-style iterative refinements [35], which aligns with the interpretation adopted in this work. A representative example is diffusion posterior sampling (DPS) [4], where  $\mathbf{x}_t$  and  $\mathbf{x}_{t+\Delta t}$  are linked through a combined update consisting of a diffusion prior term and a data-consistency term:  $s_{\theta}^*(\mathbf{x}_t, \sigma_t) - \rho \nabla_{\mathbf{x}_t} \|\mathbf{y} - \mathcal{A}(\hat{\mathbf{x}}_0(\mathbf{x}_t))\|_2^2$ , with  $\hat{\mathbf{x}}_0(\mathbf{x}_t)$  computed via Eq. 6.

From Eq. 3, the diffusion prior gradient and the likelihood gradient are statistically independent. This allows the DPS update to be rewritten as

$$\mathbf{x}'_{t-1} = \mathbf{x}_t + \sigma_t^2 s_\theta(\mathbf{x}_t, \sigma_t) + \sigma_{t-1} \mathbf{z} - \eta_t \left[ \nabla_{\mathbf{x}_0} \|\mathbf{y} - \mathcal{A}(\mathbf{x}_0)\|_2^2 \right]_{\mathbf{x}_0=\hat{\mathbf{x}}_0(\mathbf{x}_t)}. \quad (10)$$

where  $\mathbf{z} \sim \mathcal{N}(\mathbf{0}, \mathbf{I})$  and  $\eta_t$  denotes the step size.

Under our formulation, this update naturally decomposes into two decoupled operations:

1. **Expectation step:** estimate the clean mean  $\hat{\mathbf{x}}_0$  from  $\mathbf{x}_t$  using the diffusion score derived from Tweedie’s formulation;
2. **Maximization step:** refine this estimate through a single MAP-style likelihood update, followed by a re-noising operation that transitions the system to the next noise level  $\sigma_{t-1}$ .

This reinterpretation indicates that what is commonly described as posterior sampling in diffusion-based inverse problems is, in effect, a sequential E–M procedure alternating between diffusion-based estimation and data-driven optimization. By making this separation explicit, DAPS++ provides a clearer theoretical grounding and a more stable computational structure for general inverse problems, reducing reliance on explicit prior constraints and improving overall robustness.

## 4. Experiments

### 4.1. Experimental Setup

We evaluate our method using pixel-space pre-trained diffusion models on the FFHQ [4] and ImageNet [8] datasets. For the noise schedule, we adopt the POLY(-7) discretization from EDM [16]. To improve efficiency,  $\hat{\mathbf{x}}_0(\mathbf{x}_t)$  is generated using Eq. 6 while  $\sigma_t > \bar{\sigma}$ , and a single RK4 update is used once  $\sigma_t \leq \bar{\sigma}$ . Empirically, we set  $\bar{\sigma} = 10 \times \gamma$  to balance computational cost and reconstruction accuracy. The total number of neural function evaluations (NFEs) remains low because each iteration requires only one network evaluation, further reduced by an annealed step-size schedule.

We use DAPS++-50 (50 annealing steps) for FFHQ and DAPS++-100 (100 steps) for ImageNet. Each DAPS++ iteration performs 4–8 MCMC refinement steps, except for nonlinear deblurring, which requires around 50 refinement steps in the M-step. Learning rates are tuned individually for each task. Additional details regarding model configurations, samplers, and hyperparameters appear in the Appendix, along with a discussion of sampling efficiency in Fig. 5.

Because the diffusion model already captures the underlying structure and fine-scale statistics of the data distribution, it effectively denoises the input while restoring plausible high-frequency details. Since the diffusion output ap-

proximates  $\mathcal{A}(\mathbf{x}_0)$ , the residual between this prediction and the measurement  $\mathbf{y}$  is mostly dominated by noise. To ensure stable convergence and avoid overfitting to measurement noise, the injected diffusion noise at the end of each iteration must be smaller than the additive noise level. In practice, we use a noise schedule decaying from  $\sigma_{\max} = 100$  to  $\sigma_{\min} = 0.1$  with measurement noise  $\gamma = 0.05$ , which effectively suppresses overfitting and preserves structural fidelity throughout the DAPS family.

We compare our method against several state-of-the-art diffusion-based inverse problem solvers, including DAPS-1K, DAPS-100 [38], DPS [4], DDRM [17], DDNM [17], DiffPIR [40], and DCDP [18]. Note that SVD-based methods such as DDRM and DDNM apply only to linear inverse problems.

**Forward measurement operators.** We evaluate our approach on a variety of linear and nonlinear inverse problems. Linear tasks include super-resolution, Gaussian and motion deblurring, and inpainting with box or random masks. For Gaussian and motion blur, we use  $61 \times 61$  kernels with standard deviations of 3.0 and 0.5, respectively. Super-resolution employs bicubic downsampling by a factor of 4, while inpainting tasks use the standard  $128 \times 128$  box mask. Nonlinear tasks include high dynamic range (HDR) reconstruction and nonlinear deblurring, following configurations described in [38]. All measurements are corrupted by additive white noise with standard deviation  $\gamma = 0.05$ .

**Datasets and metrics.** We evaluate the proposed method on two benchmark datasets: FFHQ ( $256 \times 256$ ) [15] and ImageNet ( $256 \times 256$ ) [6]. For both datasets, 100 validation images are used for quantitative evaluation under identical conditions. To comprehensively assess reconstruction quality, we report SSIM [34], LPIPS [39], and FID [12] as our primary metrics. All methods—including ours and the baselines—are evaluated on images normalized to  $[0, 1]$  to ensure consistency and comparability across datasets.

### 4.2. Results

**Main results.** Tab.1 and Tab.2 present the quantitative comparisons against various baselines, with qualitative examples shown in Fig. 3. Across both linear and nonlinear inverse problems, our method achieves competitive—or superior—reconstruction quality with higher SSIM and lower LPIPS and FID, while requiring substantially fewer NFEs than DAPS-1K. Under identical NFE budgets, DAPS++ consistently attains higher fidelity, demonstrating the effectiveness of fully decoupling the prior and likelihood stages and avoiding overfitting in either stage. DAPS++ also shows strong robustness under heavily degraded conditions, such as bicubic  $8 \times$  super-resolution, where it can still recover meaningful structural information using only the ImageNet pre-trained model.

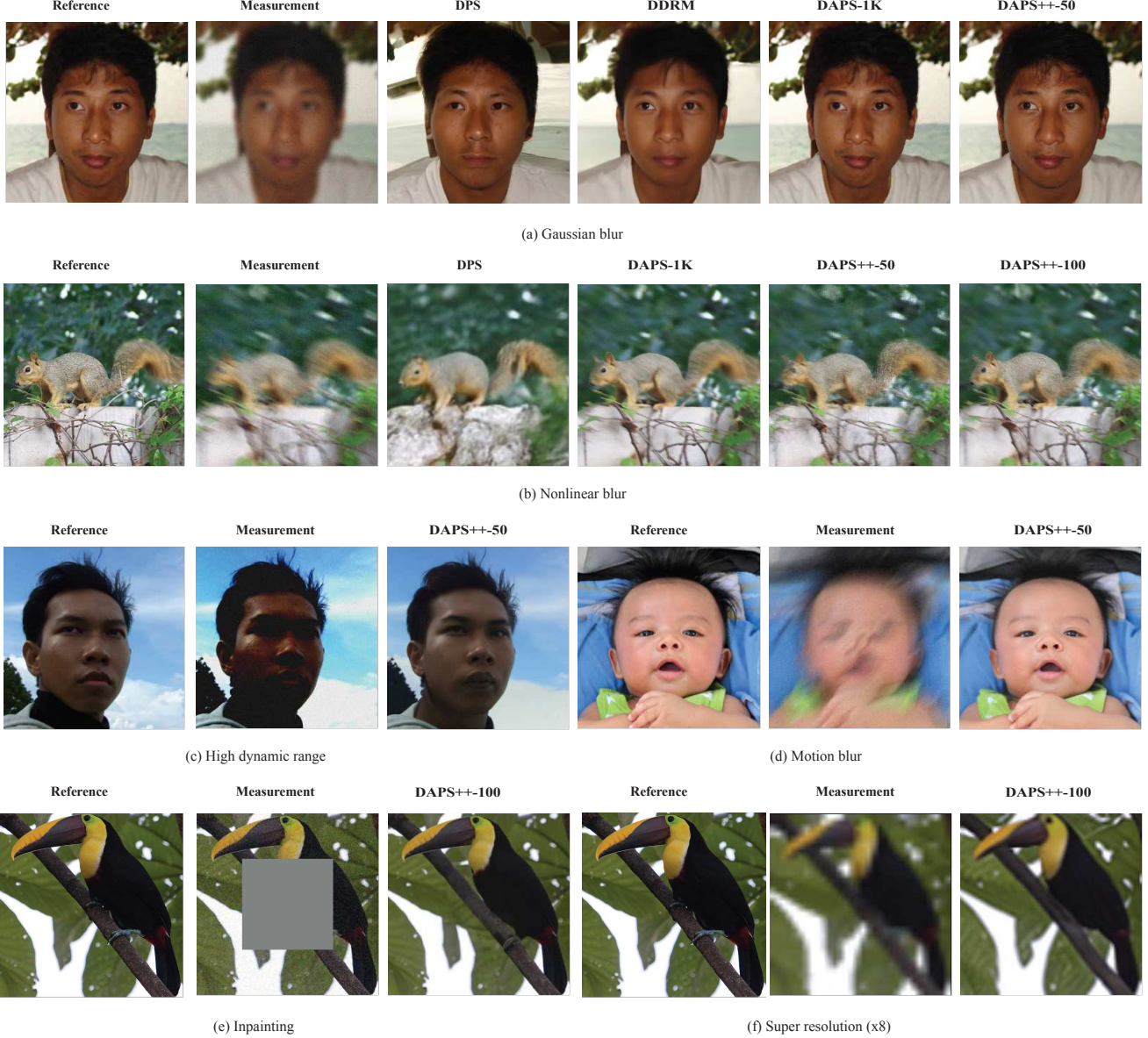


Figure 3. Qualitative results on representative inverse problems: (a) Gaussian blur reconstruction on the FFHQ-256 dataset compared with selected baselines. (b) Nonlinear blur reconstruction on ImageNet, comparing **DAPS++-50** and **DAPS++-100** alongside selected baselines. (c) High dynamic range (HDR) reconstruction on the FFHQ-256 dataset. (d) Motion blur reconstruction on the FFHQ-256 dataset. (e) Box inpainting results on ImageNet, where **DAPS++** accurately restores structural details. (f)  $8\times$  super-resolution using a pre-trained ImageNet diffusion model, demonstrating strong visual fidelity.

During the E–M updates, the optimization stages are deliberately non-overlapping. Conventional MAP-style updates in the M-step typically overfit measurement noise unless carefully regularized. In contrast, DAPS++ employs larger step sizes and fewer refinement iterations, leveraging the structure provided by the diffusion-based initialization while avoiding noise amplification. This design yields stable convergence and improved reconstruction quality at lower computational cost.

Small-step ODE solvers introduce notable discretization error when only a limited number of updates are performed. For example, DAPS-1K uses five Euler steps, resulting in an  $\mathcal{O}(\Delta t)$  error that produces a weaker initialization compared with Tweedie-based estimation. As a consequence, more MCMC iterations are needed to return to the posterior manifold. DAPS++, by directly predicting the denoised mean in the E-step, avoids this discretization bottleneck and converges more rapidly with significantly fewer

Method	SR x4		Inpainting	Gaussian Blur	Motion Blur	Nonlinear Blur	HDR
	SSIM↑ / LPIPS↓ / FID↓	SSIM↑ / LPIPS↓ / FID↓	SSIM↑ / LPIPS↓ / FID↓	SSIM↑ / LPIPS↓ / FID↓	SSIM↑ / LPIPS↓ / FID↓	SSIM↑ / LPIPS↓ / FID↓	SSIM↑ / LPIPS↓ / FID↓
DDNM	0.720 / 0.290 / 152.94	<u>0.810</u> / <u>0.162</u> / 94.66	<b>0.804</b> / 0.216 / 57.83	—	—	—	—
DDRM	<b>0.820</b> / <u>0.191</u> / 76.07	0.792 / 0.210 / 88.90	<u>0.786</u> / 0.218 / 89.40	—	—	—	—
DiffPIR	0.545 / 0.269 / 60.03	0.525 / 0.344 / 63.83	0.514 / 0.293 / 65.26	0.553 / 0.257 / 52.57	—	—	—
DCDP	0.642 / 0.333 / 92.92	0.757 / 0.167 / 42.32	0.719 / 0.282 / 82.23	0.508 / 0.384 / 115.16	<b>0.803</b> / <b>0.160</b> / <b>44.79</b>	—	—
DPS	0.591 / 0.357 / 81.05	0.727 / 0.259 / 75.56	0.647 / 0.285 / 73.33	0.588 / 0.327 / 76.82	0.648 / 0.281 / 74.27	0.693 / 0.284 / 77.61	—
DAPS-100	0.721 / 0.233 / 69.28	0.716 / 0.194 / 52.89	0.731 / 0.220 / 63.35	0.766 / 0.182 / 54.76	0.685 / 0.239 / 68.11	0.819 / 0.184 / 44.86	—
DAPS-1K	<u>0.782</u> / 0.192 / <u>55.46</u>	0.747 / 0.176 / <u>50.11</u>	<u>0.786</u> / <u>0.179</u> / <u>52.73</u>	<b>0.836</b> / <u>0.137</u> / <u>38.38</u>	<u>0.762</u> / <u>0.191</u> / <u>57.80</u>	<b>0.839</b> / <u>0.163</u> / <b>41.09</b>	—
DAPS++-50 (ours)	0.781 / <b>0.176</b> / <b>45.99</b>	<b>0.812</b> / <b>0.141</b> / <b>42.14</b>	0.784 / <u>0.171</u> / <u>51.13</u>	<u>0.829</u> / <u>0.136</u> / <b>37.86</b>	0.745 / 0.194 / 54.86	<u>0.834</u> / <u>0.169</u> / 42.30	—

Table 1. Quantitative comparison on 100 validation images of **FFHQ** across four linear and two nonlinear inverse problems. Metrics are reported as **SSIM↑ / LPIPS↓ / FID↓**. Bold indicates the best result; underlined values denote the second best. All measurements include additive Gaussian noise with  $\gamma = 0.05$ .

Method	SR x4		Inpainting	Gaussian Blur	Motion Blur	Nonlinear Blur	HDR
	SSIM↑ / LPIPS↓ / FID↓	SSIM↑ / LPIPS↓ / FID↓	SSIM↑ / LPIPS↓ / FID↓	SSIM↑ / LPIPS↓ / FID↓	SSIM↑ / LPIPS↓ / FID↓	SSIM↑ / LPIPS↓ / FID↓	SSIM↑ / LPIPS↓ / FID↓
DDNM	0.487 / 0.458 / 215.27	0.656 / 0.289 / 157.85	<b>0.650</b> / <b>0.231</b> / <b>90.83</b>	—	—	—	—
DDRM	0.652 / 0.296 / 111.20	0.602 / 0.336 / 163.67	<b>0.584</b> / 0.361 / 161.01	—	—	—	—
DiffPIR	0.443 / 0.370 / <b>106.75</b>	0.500 / 0.390 / 149.22	0.395 / 0.428 / 154.58	0.152 / 0.683 / 264.79	—	—	—
DPS	0.454 / 0.474 / 208.41	0.623 / 0.343 / 157.49	<b>0.526</b> / 0.355 / 155.61	0.542 / 0.365 / 161.40	0.520 / 0.365 / 151.53	0.349 / 0.552 / 213.76	—
DAPS-100	0.610 / 0.309 / 114.38	0.693 / 0.248 / 123.64	0.619 / 0.296 / 117.00	0.710 / 0.209 / 62.03	0.650 / 0.263 / 105.73	<b>0.810</b> / <u>0.189</u> / <b>43.17</b>	—
DAPS-1K	<u>0.638</u> / <u>0.295</u> / <u>109.13</u>	0.715 / 0.229 / 113.96	<u>0.658</u> / <u>0.268</u> / <u>107.58</u>	<b>0.769</b> / <b>0.175</b> / <b>47.09</b>	<b>0.720</b> / <u>0.212</u> / <u>75.94</u>	<b>0.824</b> / <u>0.171</u> / <u>44.65</u>	—
DAPS++-50 (ours)	<u>0.653</u> / <u>0.283</u> / 111.72	<u>0.760</u> / <u>0.208</u> / <u>113.28</u>	<b>0.666</b> / 0.269 / 117.98	0.754 / 0.185 / 57.40	0.686 / 0.234 / 85.51	0.807 / <u>0.189</u> / 46.92	—
DAPS++-100 (ours)	<b>0.661</b> / <u>0.276</u> / 114.15	<b>0.771</b> / <u>0.195</u> / <b>105.31</b>	<u>0.663</u> / 0.273 / 122.88	<u>0.763</u> / <u>0.179</u> / <u>56.05</u>	<u>0.718</u> / <u>0.211</u> / <b>75.68</b>	0.807 / 0.191 / 48.49	—

Table 2. Quantitative comparison on 100 validation images of **ImageNet** with four linear and two nonlinear tasks. Metrics follow **SSIM↑ / LPIPS↓ / FID↓**. Bold values denote the best performance; underlined entries indicate the second best. Each measurement includes additive Gaussian noise with  $\gamma = 0.05$ .

total steps. All baseline methods are evaluated on images normalized to  $[0, 1]$  to ensure consistency and comparability across datasets.

**Noise Tolerance.** DAPS++ exhibits strong robustness under increasing noise levels. As shown in Tab. 3 and Fig. 4, when  $\sigma_{\min} = 0.1$  and  $\gamma = 0.1$ , DAPS tends to overfit the noise, producing visible artifacts. In contrast, DAPS++ preserves structural fidelity and perceptual quality even as the noise level increases. As  $\gamma$  rises from 0.05 to 0.4, DAPS++ consistently exhibits stronger robustness, especially when  $\sigma_{\min}$  is matched to  $\gamma$ , demonstrating its ability to prevent overfitting. This robustness arises from the EM-style re-noising mechanism and the reduced number of refinement steps, which together prevent overfitting and maintain diffusion-driven variability.

### 4.3. Ablation Studies

**Efficiency comparison.** We assess the efficiency of DAPS++ under varying computational budgets by evaluating configurations with diffusion NFEs ranging from 20 to 200, and comparing them against DAPS variants using 50 to 1K NFEs as well as several representative baselines. All methods are evaluated in terms of single-image sampling time on an NVIDIA A100 (80GB PCIe) GPU and re-



Figure 4. Example under  $\gamma=0.1$ ,  $\sigma_{\min}=0.1$ . Comparison between (a) **DAPS++** and (b) **DAPS** for Gaussian blur shows that DAPS overfits noise, producing more artifacts in the final outputs.

construction quality using the LPIPS metric. As shown in Fig. 5, the trade-off between sampling cost and reconstruction quality consistently favors DAPS++, which achieves higher fidelity at substantially lower computational cost

Noise Level	$\gamma=0.05, \sigma_{\min}=0.1$	$\gamma=0.1, \sigma_{\min}=0.1$	$\gamma=0.2, \sigma_{\min}=0.2$	$\gamma=0.4, \sigma_{\min}=0.4$
	SSIM $\uparrow$ / LPIPS $\downarrow$			
DAPS-1K	0.786 / 0.179	0.615 / 0.330	0.410 / 0.495	0.192 / 0.633
DAPS++-50 (ours)	<b>0.784 / 0.171</b>	<b>0.728 / 0.191</b>	<b>0.674 / 0.229</b>	<b>0.579 / 0.303</b>

Table 3. Quantitative comparison of **DAPS-1K** and **DAPS++-50** under varying noise levels on the FFHQ Gaussian blur task with different  $\sigma_{\min}$  is matched to  $\gamma$ .

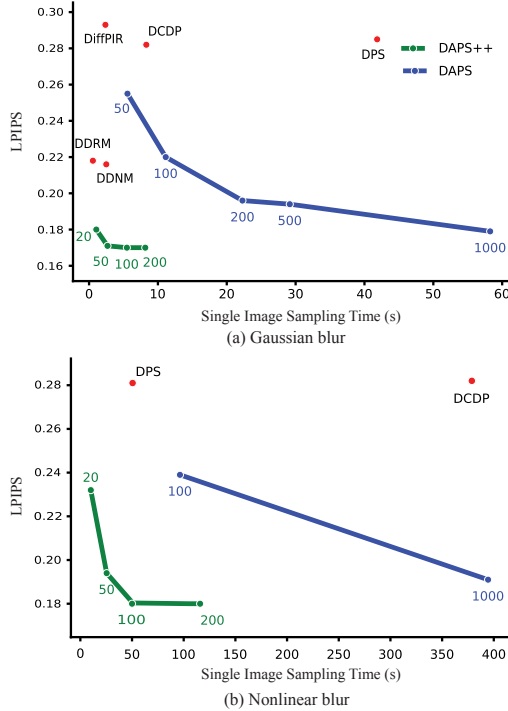


Figure 5. Evaluation of sampling time versus reconstruction quality. The x-axis denotes the per-image sampling time on an NVIDIA A100 (80GB PCIe) GPU, and the y-axis shows the LPIPS metric. Results are averaged over 100 FFHQ images for both the Gaussian blur and nonlinear blur tasks.

across both linear and nonlinear inverse problems. Even at extremely low computational settings, such as DAPS++-20, the method converges rapidly and produces competitive reconstructions for linear degradation models, suggesting that the fully decoupled formulation provides an effective path toward stable likelihood-driven refinement without relying on heavy diffusion sampling. As computational budgets increase, DAPS++ exhibits progressively improved performance while maintaining a significantly lower cost profile than diffusion-based alternatives that interleave prior and likelihood updates at every timestep. Overall, these results demonstrate that DAPS++ achieves a favorable balance between accuracy and efficiency, making it a scalable and practical solution for real-time or resource-limited inverse imaging applications.

**Hyperparameter choice.** Two hyperparameters play a central role in DAPS++: the threshold noise level  $\bar{\sigma}$  and the polynomial scheduler exponent. Both parameters directly influence reconstruction quality, particularly when the number of sampling steps is limited and the interaction between diffusion initialization and likelihood refinement becomes more sensitive. The threshold  $\bar{\sigma}$  determines when Tweedie-based estimation transitions to a higher-order ODE solver within the diffusion process, allowing efficient denoising at large noise levels and producing a reliable initialization with only a few high-order ODE evaluations. However, even under small noise settings, purely diffusion-generated estimates without data-driven refinement will drift away from the measurement to the next E-step. Therefore, after the higher-order solver step, we still apply an M-step update at the end of the annealing schedule to correct this deviation.

The polynomial scheduler exponent governs the decay rate of the noise levels during annealing and becomes especially important in low-step regimes (e.g., 20–50 steps), as it controls the trade-off between convergence stability and refinement strength. A slower decay stabilizes the M-step updates but introduces more high-noise transitions, which may reduce the effectiveness of likelihood refinement. A faster decay generally accelerates convergence and is often preferred in practice, provided that the M-step remains numerically stable. A comprehensive sensitivity analysis for these hyperparameters, along with practical tuning guidelines, is provided in the Appendix.

## 5. Conclusion

In this work, we revisit the underlying mechanism of diffusion-based inverse problem solvers and propose an expectation–maximization (E–M) style formulation that makes explicit the separation between the diffusion and data-consistency stages. Based on this perspective, we develop **DAPS++**, a fully decoupled framework that substantially improves sampling efficiency while preserving high reconstruction fidelity. The diffusion stage functions as a prior-driven initialization on a flat manifold, whereas the data-consistency stage performs likelihood-guided refinement independent of the diffusion process. This separation offers a clearer Bayesian interpretation of diffusion-based inference and provides an explanation for the empirical behavior of existing approaches. Across both linear and nonlinear imaging tasks, DAPS++ achieves strong performance using only a fraction of the function evaluations required by conventional methods, establishing an efficient and scalable foundation for future research in diffusion-based inverse problems.

## References

[1] Gabriel Cardoso, Yazid Janati El Idrissi, Sylvain Le Corff, and Eric Moulines. Monte carlo guided diffusion for Bayesian linear inverse problems. 2024. 1

[2] Jooyoung Choi, Sungwon Kim, Yonghyun Jeong, Youngjune Gwon, and Sungroh Yoon. Ilvr: Conditioning method for denoising diffusion probabilistic models. In *Proceedings of the IEEE/CVF International Conference on Computer Vision (ICCV)*, pages 14367–14376, 2021. 2

[3] Hyungjin Chung, Byeongsu Sim, Dohoon Ryu, and Jong Chul Ye. Improving diffusion models for inverse problems using manifold constraints. *Advances in Neural Information Processing Systems*, 35:25683–25696, 2022. 2

[4] Hyungjin Chung, Jeongsol Kim, Michael T Mccann, Marc L Klasky, and Jong Chul Ye. Diffusion posterior sampling for general noisy inverse problems. 2023. 1, 2, 4, 5

[5] Masoumeh Dashti and Andrew M Stuart. The bayesian approach to inverse problems. In *Handbook of uncertainty quantification*, pages 1–118. Springer, 2015. 1

[6] Jia Deng, Wei Dong, Richard Socher, Li-Jia Li, Kai Li, and Li Fei-Fei. Imagenet: A large-scale hierarchical image database. In *2009 IEEE conference on computer vision and pattern recognition*, pages 248–255. Ieee, 2009. 5

[7] Nicolas Dey, Laure Blanc-Feraud, Christophe Zimmer, Pascal Roux, Zvi Kam, Jean-Christophe Olivo-Marin, and Josiane Zerubia. Richardson–lucy algorithm with total variation regularization for 3d confocal microscope deconvolution. *Microscopy research and technique*, 69(4):260–266, 2006. 1

[8] Prafulla Dhariwal and Alexander Nichol. Diffusion models beat gans on image synthesis. *Advances in neural information processing systems*, 34:8780–8794, 2021. 5

[9] Berthy T Feng, Jamie Smith, Michael Rubinstein, Hui-wen Chang, Katherine L Bouman, and William T Freeman. Score-based diffusion models as principled priors for inverse imaging. In *Proceedings of the IEEE/CVF International Conference on Computer Vision*, pages 10520–10531, 2023. 1

[10] DA Fish, AM Brinicombe, ER Pike, and JG Walker. Blind deconvolution by means of the richardson–lucy algorithm. *Journal of the Optical Society of America A*, 12(1):58–65, 1995. 1

[11] Alison L Gibbs and Francis Edward Su. On choosing and bounding probability metrics. *International statistical review*, 70(3):419–435, 2002. 1

[12] Martin Heusel, Hubert Ramsauer, Thomas Unterthiner, Bernhard Nessler, and Sepp Hochreiter. Gans trained by a two time-scale update rule converge to a local nash equilibrium. *Advances in neural information processing systems*, 30, 2017. 5

[13] Jonathan Ho, Ajay Jain, and Pieter Abbeel. Denoising diffusion probabilistic models. *Advances in neural information processing systems*, 33:6840–6851, 2020. 1, 2

[14] Ajil Jalal, Marius Arvinte, Giannis Daras, Eric Price, Alexandros G Dimakis, and Jon Tamir. Robust compressed sensing mri with deep generative priors. *Advances in neural information processing systems*, 34:14938–14954, 2021. 1

[15] Tero Karras, Samuli Laine, and Timo Aila. A style-based generator architecture for generative adversarial networks. In *Proceedings of the IEEE/CVF conference on computer vision and pattern recognition*, pages 4401–4410, 2019. 5

[16] Tero Karras, Miika Aittala, Timo Aila, and Samuli Laine. Elucidating the design space of diffusion-based generative models. *Advances in neural information processing systems*, 35:26565–26577, 2022. 1, 2, 5, 3, 4

[17] Bahjat Kawar, Michael Elad, Stefano Ermon, and Jiaming Song. Denoising diffusion restoration models. *Advances in neural information processing systems*, 35:23593–23606, 2022. 2, 5

[18] Xiang Li, Soo Min Kwon, Shijun Liang, Ismail R Alkhouri, Saiprasad Ravishankar, and Qing Qu. Decoupled data consistency with diffusion purification for image restoration. *arXiv preprint arXiv:2403.06054*, 2024. 1, 2, 5

[19] Cheng Lu, Yuhao Zhou, Fan Bao, Jianfei Chen, Chongxuan Li, and Jun Zhu. Dpm-solver: A fast ode solver for diffusion probabilistic model sampling in around 10 steps. *Advances in neural information processing systems*, 35:5775–5787, 2022. 1

[20] Cheng Lu, Yuhao Zhou, Fan Bao, Jianfei Chen, Chongxuan Li, and Jun Zhu. Dpm-solver++: Fast solver for guided sampling of diffusion probabilistic models. *Machine Intelligence Research*, pages 1–22, 2025. 1

[21] LB Lucy. Optimum strategies for inverse problems in statistical astronomy. *Astronomy and Astrophysics (ISSN 0004-6361)*, vol. 289, no. 3, p. 983–994, 289:983–994, 1994. 1

[22] Michael Lustig, David Donoho, and John M Pauly. Sparse mri: The application of compressed sensing for rapid mr imaging. *Magnetic Resonance in Medicine: An Official Journal of the International Society for Magnetic Resonance in Medicine*, 58(6):1182–1195, 2007. 1

[23] Oliver Porth, Koushik Chatterjee, Ramesh Narayan, Charles F Gammie, Yosuke Mizuno, Peter Anninos, John G Baker, Matteo Bugli, Chi-kwan Chan, Jordy Davelaar, et al. The event horizon general relativistic magnetohydrodynamic code comparison project. *The Astrophysical Journal Supplement Series*, 243(2):26, 2019. 1

[24] Viraj Shah and Chinmay Hegde. Solving linear inverse problems using gan priors: An algorithm with provable guarantees. In *2018 IEEE international conference on acoustics, speech and signal processing (ICASSP)*, pages 4609–4613. IEEE, 2018. 1

[25] Bowen Song, Soo Min Kwon, Zecheng Zhang, Xinyu Hu, Qing Qu, and Liyue Shen. Solving inverse problems with latent diffusion models via hard data consistency. In *The Twelfth International Conference on Learning Representations*, 2024. 2, 3

[26] Jiaming Song, Chenlin Meng, and Stefano Ermon. Denoising diffusion implicit models. 2021. 1

[27] Yang Song and Stefano Ermon. Generative modeling by estimating gradients of the data distribution. *Advances in neural information processing systems*, 32, 2019. 1, 2

[28] Yang Song and Stefano Ermon. Improved techniques for training score-based generative models. *Advances in neural information processing systems*, 33:12438–12448, 2020.

[29] Yang Song, Jascha Sohl-Dickstein, Diederik P Kingma, Abhishek Kumar, Stefano Ermon, and Ben Poole. Score-based generative modeling through stochastic differential equations. In *ICLR*, 2021. [1](#), [2](#)

[30] Yang Song, Liyue Shen, Lei Xing, and Stefano Ermon. Solving inverse problems in medical imaging with score-based generative models. 2022. [1](#)

[31] Andrew M Stuart. Inverse problems: a bayesian perspective. *Acta numerica*, 19:451–559, 2010. [1](#)

[32] Albert Tarantola. *Inverse problem theory and methods for model parameter estimation*. SIAM, 2005. [1](#)

[33] Yinhuai Wang, Jiwen Yu, and Jian Zhang. Zero-shot image restoration using denoising diffusion null-space model. In *The Eleventh International Conference on Learning Representations*, 2023. [2](#)

[34] Zhou Wang, Alan C Bovik, Hamid R Sheikh, and Eero P Simoncelli. Image quality assessment: from error visibility to structural similarity. *IEEE transactions on image processing*, 13(4):600–612, 2004. [5](#)

[35] Tongda Xu, Xiyan Cai, Xinjie Zhang, Xingtong Ge, Dailan He, Ming Sun, Jingjing Liu, Ya-Qin Zhang, Jian Li, and Yan Wang. Rethinking diffusion posterior sampling: From conditional score estimator to maximizing a posterior. In *The Thirteenth International Conference on Learning Representations*, 2025. [2](#), [4](#)

[36] Xingyu Xu and Yuejie Chi. Provably robust score-based diffusion posterior sampling for plug-and-play image reconstruction. *Advances in Neural Information Processing Systems*, 37:36148–36184, 2024. [2](#)

[37] Lingxiao Yang, Shutong Ding, Yifan Cai, Jingyi Yu, Jingya Wang, and Ye Shi. Guidance with spherical gaussian constraint for conditional diffusion. In *Proceedings of the 41st International Conference on Machine Learning*. JMLR.org, 2024. [2](#)

[38] Bingliang Zhang, Wenda Chu, Julius Berner, Chenlin Meng, Anima Anandkumar, and Yang Song. Improving diffusion inverse problem solving with decoupled noise annealing. In *Proceedings of the Computer Vision and Pattern Recognition Conference*, pages 20895–20905, 2025. [1](#), [2](#), [5](#), [3](#)

[39] Richard Zhang, Phillip Isola, Alexei A Efros, Eli Shechtman, and Oliver Wang. The unreasonable effectiveness of deep features as a perceptual metric. In *Proceedings of the IEEE conference on computer vision and pattern recognition*, pages 586–595, 2018. [5](#)

[40] Yuanzhi Zhu, Kai Zhang, Jingyun Liang, Jiezhang Cao, Bihan Wen, Radu Timofte, and Luc Van Gool. Denoising diffusion models for plug-and-play image restoration. In *Proceedings of the IEEE/CVF conference on computer vision and pattern recognition*, pages 1219–1229, 2023. [5](#)

# DAPS++: Rethinking Diffusion Inverse Problems with Decoupled Posterior Annealing

## Supplementary Material

### 6. Theoretical Analysis

#### 6.1. Lipschitz Analysis of Prior–Likelihood Interaction

To establish the negligible contribution of the prior gradient in high-noise regimes, we provide a Lipschitz-bound analysis quantifying the relative magnitudes of the likelihood and prior terms. We first introduce standard assumptions.

##### Assumptions.

- A1.** The score function  $\nabla_{\mathbf{x}_t} \log p_t(\mathbf{x}_t; \sigma_t)$  is  $L_{\sigma_t}$ -Lipschitz continuous with  $L_{\sigma_t} \leq C/\sigma_t^2$  for some constant  $C > 0$ , following standard smoothed density properties.
- A2.** The measurement operator  $\mathcal{A}$  is linear. We denote its smallest *non-zero* singular value as  $\sigma_{\min}^+(\mathcal{A}) > 0$ .
- A3.** The observation noise variance  $\gamma^2$  is finite, with  $\sigma_t \gg \gamma$  in high-noise regimes.

**Prior negligibility via Lipschitz bounds.** Consider the linear inverse problem  $\mathbf{y} = \mathcal{A}\mathbf{x}_0 + \boldsymbol{\epsilon}$  where  $\boldsymbol{\epsilon} \sim \mathcal{N}(0, \gamma^2 \mathbf{I})$  and we define the measurement residual

$$\mathbf{r}_t := \mathbf{y} - \mathcal{A}\hat{\mathbf{x}}_0(\mathbf{x}_t). \quad (11)$$

Under Assumptions **A1–A3**, the gradient ratio satisfies

$$\kappa_t \geq \frac{\sigma_{\min}^+(\mathcal{A})}{\gamma^2 C} \sigma_t \|\mathbf{r}_t\|. \quad (12)$$

When  $\sigma_t/\gamma \gg 1$  and  $\|\mathbf{r}_t\| = \Theta(1)$ , we obtain  $\kappa_t \gg 1$ , implying dominance of the likelihood gradient.

**Proof.** We upper-bound the prior gradient and lower-bound the likelihood gradient.

(i) *Upper bound on the prior gradient.* From Assumption **A1**, the magnitude of the score is bounded by

$$\|\nabla_{\mathbf{x}_t} \log p_t(\mathbf{x}_t; \sigma_t)\| \lesssim \frac{C}{\sigma_t}. \quad (13)$$

(ii) *Lower bound on the likelihood gradient.* Using the Gaussian likelihood and Tweedie’s formula, the likelihood score is:

$$\nabla_{\mathbf{x}_t} \log p_t(\mathbf{y} | \mathbf{x}_t; \sigma_t) = \frac{1}{\gamma^2} \mathcal{A}^\top \mathbf{r}_t + O(\sigma_t). \quad (14)$$

Since  $\mathbf{r}_t$  lies in the measurement space (the range of  $\mathcal{A}$  plus noise), the back-projection via  $\mathcal{A}^\top$  is bounded by the smallest non-zero singular value acting on the effective residual.

Thus:

$$\|\nabla_{\mathbf{x}_t} \log p_t(\mathbf{y} | \mathbf{x}_t; \sigma_t)\| \geq \frac{\sigma_{\min}^+(\mathcal{A})}{\gamma^2} \|\mathbf{r}_t\|. \quad (15)$$

(iii) *Lower bound on gradient ratio.* Combining (13) and (15),

$$\kappa_t \gtrsim \frac{\sigma_{\min}^+(\mathcal{A})}{\gamma^2 C} \sigma_t \|\mathbf{r}_t\|, \quad (16)$$

establishing (12).  $\square$

**Implications.** This analysis rigorously justifies the observation that the prior gradient contributes negligibly in high-noise regimes. For standard EDM schedulers in DAPS with  $\sigma_{\max} \approx 100$  and low observation noise ( $\gamma \approx 0.01$ ), the gradient ratio reaches magnitudes of  $\kappa_t \approx 10^6$ , rendering the prior term mathematically insignificant during early sampling. As illustrated in Fig. 1, this dominance persists throughout the diffusion process, where the likelihood gradient continues to outweigh the prior contribution even at the minimal noise levels ( $\sigma_{\min} \approx 0.1$ ). Consequently, even for ill-posed problems where  $\mathcal{A}$  has a null space, the likelihood gradient operates in the row space with such high magnitude (scaled by  $1/\gamma^2$ ) that it dictates the update direction, validating the omission of the prior in the time-marginal step.

### 6.2. MCMC sampling with warm start

When applying Markov chain Monte Carlo (MCMC), an informative initial state significantly improves both convergence speed and numerical accuracy. As shown in Fig 6, different initialization strategies—including pure-noise initialization, high-order ODE-based initialization, and Tweedie-based estimation—are evaluated under identical MCMC settings (learning rate  $1 \times 10^{-3}$ , two refinement steps, and a  $4 \times$  downsampling operator). All schemes rapidly approach the measurement-consistent solution; however, the warm start obtained from Tweedie’s estimator produces notably smoother updates with reduced oscillation. After the MCMC refinement step, the Tweedie-initialized trajectories exhibit markedly fewer high-frequency artifacts compared with those initialized via higher-order ODE solvers, demonstrating its advantage as a stable and noise-robust initialization method.

### 7. Detailed Algorithm Implementation

To provide a comprehensive structural overview of the proposed framework, we present the complete pseudocode

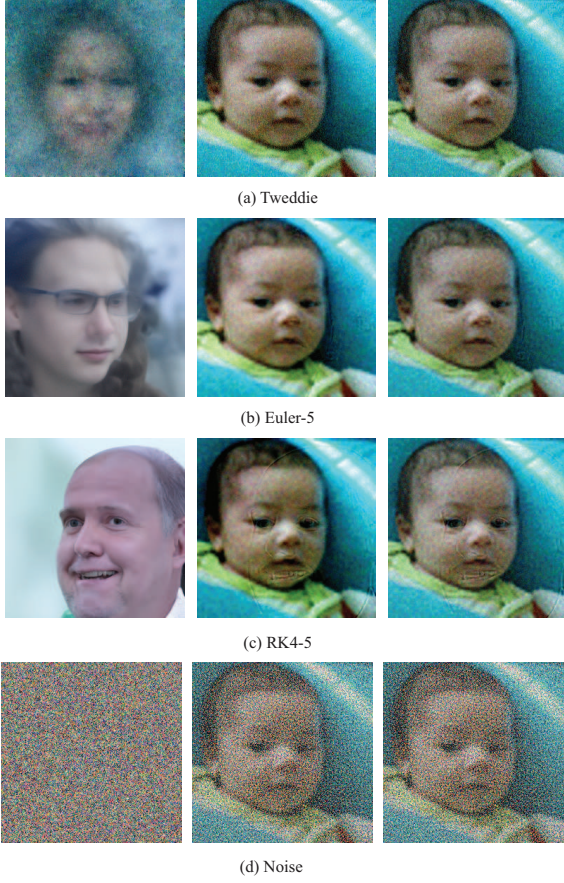


Figure 6. Visualization of 2-step MCMC iterations for  $4 \times$  down-sampling under different initialization setups. Subfigures (a)–(c) are initialized at  $\sigma_{\max} = 100$  using: (a) Tweedie’s formula, (b) a 5-step Euler ODE solver, and (c) a 5-step RK-4 ODE solver. For comparison, (d) shows standard pure noise initialization at  $\sigma = 1$ .

for DAPS++ in Algorithm 1. This outlines the heterogeneous decomposition strategy, transitioning from the prior-dominant generation in Stage 1 to the likelihood-dominant refinement in Stage 2.

## 8. Discussions

### 8.1. Sampling Efficiency

Sampling efficiency is a critical factor for diffusion-based inverse problem solvers. The computational cost of these methods depends heavily on both the number of neural function evaluations (NFEs) and the refinement steps performed at each iteration. In Tab. 4, we summarize the ODE steps, annealing steps, refinement steps, and resulting NFE budgets for several pixel-space baseline methods and for DAPS under multiple configurations, along with the corresponding single-image sampling times on FFHQ-256, compared against DAPS++. As shown, DAPS++ achieves substantially higher efficiency than existing baselines, de-

---

### Algorithm 1 DAPS++ Inference with E–M Alternating Refinement

---

**Input:** Measurement  $\mathbf{y}$ , operator  $\mathcal{A}$ , effective noise variance  $\gamma^2$ , diffusion score  $s_\theta$ , noise schedule  $\{\sigma_t\}$ , threshold  $\bar{\sigma}$ , refinement steps  $J$ , step sizes  $\{\eta_j\}$ , total E–M cycles  $K$ .

**Output:** Final reconstruction  $\hat{\mathbf{x}}_0$ .

```

1: Initialize  $x_{\text{in}}^{(0)} \sim \mathcal{N}(\mathbf{0}, \sigma_{\max}^2 \mathbf{I})$ .
2: for  $k = 1$  to  $K$  do
3:   /* E-step: One-shot diffusion initialization */
4:   if  $\sigma_{\text{in}} > \bar{\sigma}$  then
5:      $\hat{\mathbf{x}}_0^{(k)} \leftarrow x_{\text{in}}^{(k-1)} + \sigma_{\text{in}}^2 s_\theta(x_{\text{in}}^{(k-1)}, \sigma_{\text{in}})$ 
6:   else
7:      $\hat{\mathbf{x}}_0^{(k)} \leftarrow \text{ODESolver}(x_{\text{in}}^{(k-1)}, \sigma_{\text{in}})$ 
8:   end if
9:   /* M-step: Likelihood-driven refinement */
10:   $z^{(0)} \leftarrow \hat{\mathbf{x}}_0^{(k)}$ 
11:  for  $j = 1$  to  $J$  do
12:     $\mathbf{r}^{(j-1)} \leftarrow \mathbf{y} - \mathcal{A}(z^{(j-1)})$ 
13:     $\nabla_z \mathcal{L} \leftarrow \frac{1}{\gamma^2} \text{VJP}_{\mathcal{A}}(z^{(j-1)}, \mathbf{r}^{(j-1)})$ 
14:    Sample  $\xi_j \sim \mathcal{N}(\mathbf{0}, \mathbf{I})$ 
15:     $z^{(j)} \leftarrow z^{(j-1)} + \eta_j \nabla_z \mathcal{L} + \sqrt{2\eta_j} \xi_j$  {ULA refinement}
16:  end for
17:   $\tilde{\mathbf{x}}_0^{(k)} \leftarrow z^{(J)}$ 
18:  /* Re-noising to start next E-step */
19:  Sample  $\epsilon_k \sim \mathcal{N}(\mathbf{0}, \mathbf{I})$ 
20:   $x_{\text{in}}^{(k)} \leftarrow \tilde{\mathbf{x}}_0^{(k)} + \sigma_k \epsilon_k$ 
21: end for
22: return  $\hat{\mathbf{x}}_0 \leftarrow \tilde{\mathbf{x}}_0^{(K)}$ 

```

---

livering competitive performance even with very low NFE budgets.

### 8.2. Regarding Phase Retrieval

DAPS has demonstrated strong performance on the phase retrieval task compared with other baselines. However, this advantage is not consistently maintained across the entire dataset. As illustrated in Fig. 7, the variance of failure cases among the top 100 images from the FFHQ test set remains significant. These failures primarily stem from the nonlinear frequency-domain measurement operator, which interacts unfavorably with the pixel-domain initialization produced by the diffusion prior. A trajectory comparison of the diffusion output  $\hat{\mathbf{x}}_0$  in Fig. 8 further shows that DAPS++ exhibits more stable refinement behavior and achieves more reliable reconstructions under the same experimental conditions. Despite this challenge, DAPS++ achieves performance comparable to DAPS-4K while using substantially fewer sampling steps, and it exhibits a noticeably lower failure rate. This highlights that DAPS++ does not introduce

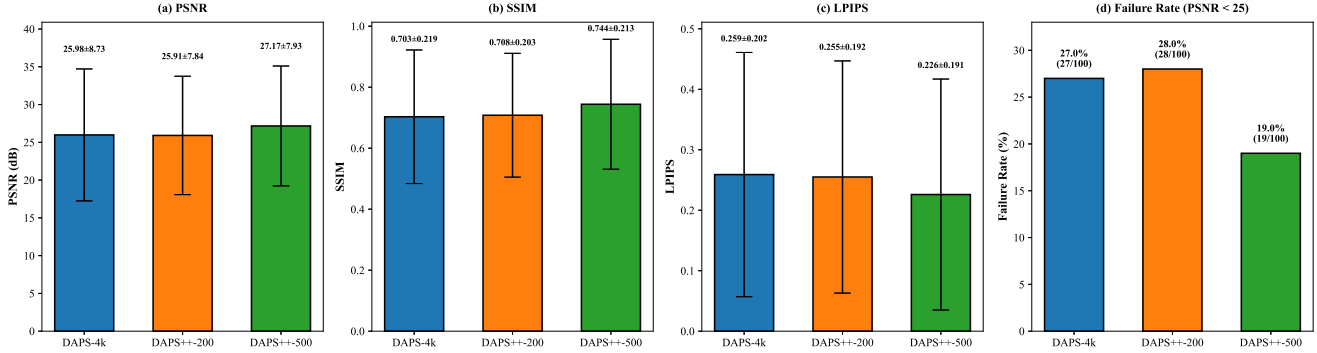


Figure 7. Phase retrieval results using the top 100 images from the FFHQ test dataset. (a) PSNR, (b) SSIM, and (c) LPIPS statistics (mean  $\pm$  standard deviation) show that DAPS++ achieves reconstruction quality comparable to DAPS-4K while requiring substantially fewer sampling steps. (d) Failure rate (PSNR  $< 25$ ) shows that instability arises from the nonlinear frequency-domain measurement operator.

Configuration	ODE/Sampling Steps	Annealing Steps	Refinement Steps	NFE	Seconds/Image
DPS	—	—	1	1000	40.90
DDRM	—	—	—	20	0.58
DiffPIR	—	—	—	100	2.41
DAPS-100	2	50	100	100	6.26
DAPS-1K	5	200	100	1000	38.10
DAPS++-20	1	20	2	40	0.89
DAPS++-50	1	50	2	100	2.31
DAPS++-100	1	100	2	200	4.62
DAPS++-200	1	200	2	400	9.25

Table 4. Sampling time of DAPS on the super-resolution task with FFHQ-256 based on  $\bar{\sigma} = 0.5$ . Reported values denote non-parallel single-image sampling time on the FFHQ-256 dataset using one NVIDIA A100 PCIe 80GB GPU.

mechanisms that address frequency-domain nonlinearities, and its behavior remains constrained in the same way as DAPS. However, with more annealing steps, the initialization has a higher chance of producing a sample closer to the true solution under a longer noise schedule.

### 8.3. Future Directions

By decoupling the solution into two iterative and independent stages, our framework avoids the complex requirement of treating the likelihood term  $p(\mathbf{y} \mid \hat{\mathbf{x}}_0(\mathbf{x}_t))$  as an intrinsic part of the diffusion-induced probability manifold. Instead, each stage can be analyzed and optimized in isolation. Specifically, the optimization phase (M-step) is liberated from the constraints of maintaining time-marginal consistency or strictly adhering to the diffusion trajectory. This independence provides a more flexible and theoretically robust foundation for applying diffusion models to measurement-driven reconstruction.

Consequently, this formulation naturally extends to complex, non-Gaussian noise models—such as Poisson or Speckle noise—which have historically been difficult to incorporate into coupled diffusion updates. Since the diffu-

sion model serves primarily to provide initialization and regularize the feasible solution space, such noise distributions become mathematically tractable. Future work will explore leveraging this decoupled architecture to handle these diverse noise models in a principled and elegant manner.

## 9. Experimental Details

We follow the forward measurement operators utilized in DAPS [38] and Resample [25], establishing a unified evaluation protocol for general linear and nonlinear inverse problems.

### 9.1. Final Refinement via RK4 Solver

To achieve high-fidelity reconstruction, we introduce a final refinement stage subsequent to the initial sampling process (which operates in the regime  $\sigma_t \leq \bar{\sigma}$ ). Specifically, we adopt the formulation from Karras et al. [16] (EDM) with  $\alpha_t \equiv 1$  (Variance Exploding SDE) and perform deterministic refinement by integrating the probability-flow ODE. The

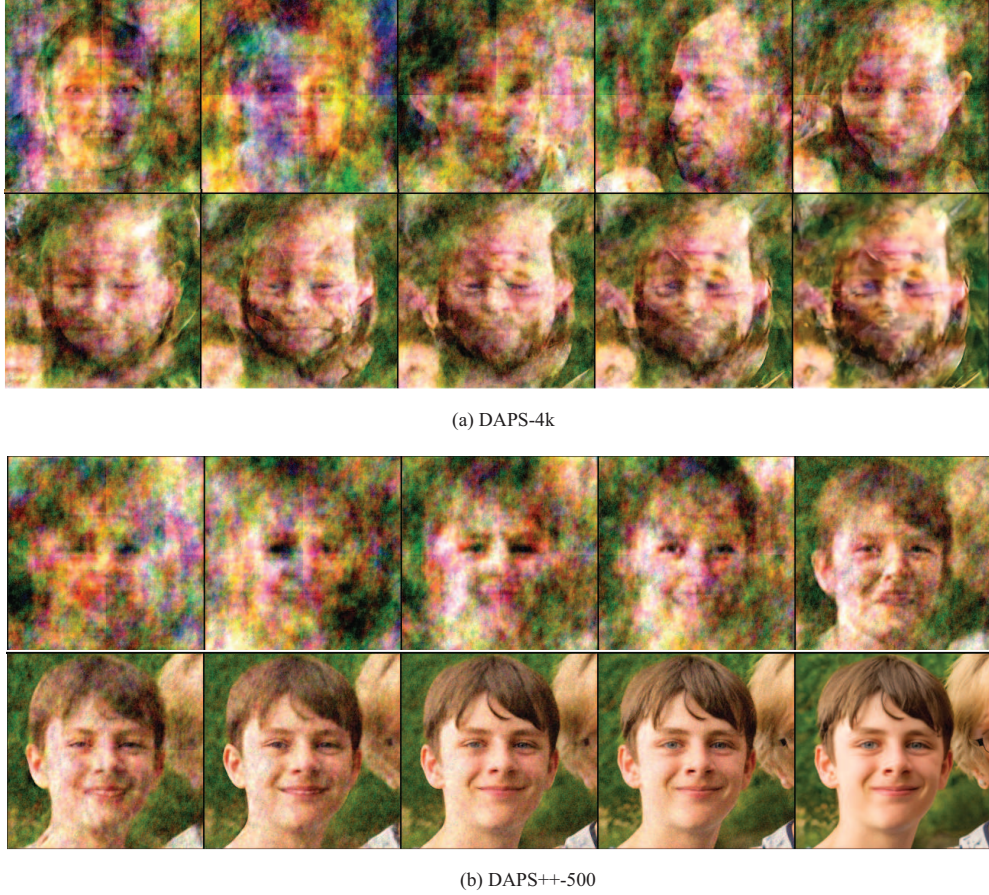


Figure 8. Visualization of the trajectory of diffusion outputs in the phase retrieval task for (a) DAPS-4K and (b) DAPS++-500.

drift term  $\mathbf{f}(\mathbf{x}_t, \sigma_t)$  governing this trajectory is defined as

$$\mathbf{f}(\mathbf{x}_t, \sigma_t) = -\dot{\sigma}_t \sigma_t s_\theta(\mathbf{x}_t, \sigma_t), \quad (17)$$

where  $s_\theta(\mathbf{x}_t, \sigma_t) \approx \nabla_{\mathbf{x}_t} \log p_t(\mathbf{x}_t)$  denotes the diffusion model’s score estimate. We employ a fourth-order Runge–Kutta (RK4) solver to integrate this ODE specifically for these final refinement steps. Given the current state  $\mathbf{x}_t$  and noise level  $\sigma_t$ , a single RK4 update with step size  $h$  is computed as

$$\begin{aligned} k_1 &= \mathbf{f}(\mathbf{x}_t, \sigma_t), \\ k_2 &= \mathbf{f}\left(\mathbf{x}_t + \frac{h}{2}k_1, \sigma_t + \frac{h}{2}\dot{\sigma}_t\right), \\ k_3 &= \mathbf{f}\left(\mathbf{x}_t + \frac{h}{2}k_2, \sigma_t + \frac{h}{2}\dot{\sigma}_t\right), \\ k_4 &= \mathbf{f}(\mathbf{x}_t + hk_3, \sigma_t + h\dot{\sigma}_t), \\ \mathbf{x}_{t-h} &= \mathbf{x}_t + \frac{h}{6}(k_1 + 2k_2 + 2k_3 + k_4). \end{aligned} \quad (18)$$

To discretize the time variable during this refinement phase, we employ the polynomial interpolation schedule from EDM [16]. For the  $i$ -th step among  $N$  total steps, the dis-

cretized time  $t_i$  is determined by

$$t_i = t_{\min} + (t_1 - t_{\min}) \left( \frac{i}{N-1} \right)^\rho. \quad (19)$$

While standard diffusion training typically utilizes  $\rho = 7$  and  $t_{\min} = 0.02$ , we tailor the schedule for the inference phase of DAPS++ (specifically with  $\gamma = 0.05$ ) to better suit the refinement requirements in the inverse problem space. Accordingly, we set  $\rho = -7$  to induce a faster decay of the noise level, thereby concentrating a greater density of discretization steps within the small-noise regime, as illustrated in Fig. 9. With this schedule, given the refinement threshold  $\bar{\sigma} = 0.5$ , approximately 30% of the total sampling steps are allocated to the refinement stage ( $\sigma_t \leq \bar{\sigma}$ ), ensuring detailed reconstruction.

## 9.2. Hyperparameter Choice

To evaluate the proposed method across general linear and nonlinear inverse problems, we maintain a unified hyperparameter setting to demonstrate robustness. Detailed configurations for all tasks—including Super-Resolution (4 $\times$ ),

Algorithm	Params	SR 4×	Inpainting	Gauss. Deblur	Motion Deblur	Nonlinear Deblur	HDR
<b>DAPS</b>	$\eta_0$	1e-4	1e-4	1e-4	5e-5	5e-5	2e-5
	$\delta$	1e-2	1e-2	1e-2	1e-2	1e-2	1e-2
	Steps	100	100	100	100	100	100
<b>DAPS++ (Ours)</b>	$\eta_0$	1e-3	1e-4	1e-4	1e-4	1e-5	2.5e-5
	$\delta$	1e-2	1e-2	1e-2	1e-2	1e-2	1e-2
	Steps	<b>2</b>	<b>5</b>	<b>8</b>	<b>8</b>	<b>50</b>	<b>5</b>

Table 5. **Hyperparameter comparison between DAPS and DAPS++.** We list the step size  $\eta_0$ , noise scale  $\delta$ , and total sampling steps. Note that while DAPS requires 100 steps for all tasks, DAPS++ achieves efficient reconstruction with significantly fewer steps (e.g., 2 steps for Super-Resolution).

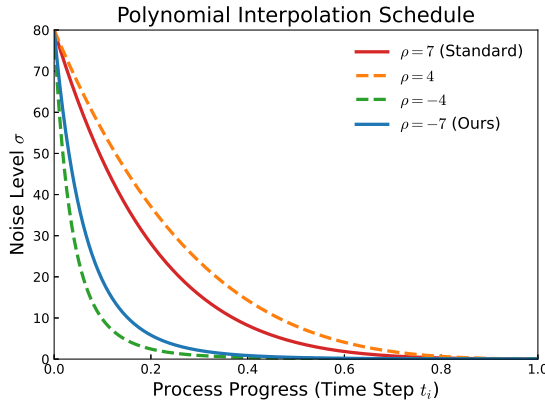


Figure 9. **Polynomial interpolation schedules.** The standard  $\rho = 7$  (red) maintains high noise levels, whereas our  $\rho = -7$  (blue) accelerates decay. This allocates more steps to the small-noise regime, crucial for detailed refinement in inverse problems.

Inpainting, Deblurring (Gaussian/Motion/Nonlinear), and High Dynamic Range (HDR)—are summarized in Tab. 5, where we provide a direct comparison with the baseline DAPS [38].

**Efficiency and NFEs.** For the annealing sampling process, we strictly limit computation to a single-step solver per time step. Unlike methods that require multiple gradient steps or extensive MCMC transitions at each noise level, our approach achieves fast and robust reconstruction with minimal computational overhead. As shown in Tab. 5, while the original DAPS requires a fixed budget of 100 MCMC steps for all tasks, DAPS++ significantly reduces the inference cost without compromising quality.

**Annealing Steps for Different Datasets.** As reported in Tab. 2 and Tab. 1, we adjust the total number of annealing steps ( $K$ ) based on the dataset complexity. Specifically, we employ a higher number of steps for ImageNet compared to FFHQ. This increase is necessitated by the significantly higher semantic diversity and manifold complexity of ImageNet, which requires a finer discretization

of the reverse trajectory to prevent the sampling path from diverging. Conversely, FFHQ, being a domain-specific face dataset with lower entropy, allows for faster convergence with fewer steps.

**General Parameters and Decay Schedule.** The step size  $\eta_0$  and noise level  $\delta$  are tuned per task to balance data consistency and perceptual quality. For the step size  $\eta_t$  at timestep  $t$ , we adopt a linear decay scheme defined as:

$$\eta_t = \eta_0 \left[ \delta + \frac{t}{T}(1 - \delta) \right], \quad (20)$$

where  $\delta$  represents the decay ratio and  $T$  is the starting timestep. Furthermore, regarding the measurement noise parameter  $\gamma$ , we treat it as an effective noise level rather than strictly adhering to the physical ground truth. Regardless of the true noise level variation (e.g., ranging from  $\gamma = 0.05$  to  $0.4$ ), we consistently set the hyperparameter to  $\gamma = 0.01$  to achieve better empirical performance and stability during the reconstruction process.

## 10. More Ablation Results

We present additional ablation studies on the choice of  $\bar{\sigma}$  and the polynomial exponent  $\rho$  in the noise schedule. Results across several inverse problems are summarized in Tab. 6 and Tab. 7, evaluated under identical measurement noise levels. Illustrative examples are provided in Fig. 10 and Fig. 11.

As shown in Tab. 6, using a larger  $\bar{\sigma}$  increases the number of required NFEs but does not yield noticeable improvements in reconstruction quality; in some tasks, it even slightly degrades performance due to excessive early-stage denoising. Conversely, a smaller  $\bar{\sigma}$  tends to improve SSIM but may oversuppress fine structures, reducing perceptual fidelity.

For the polynomial schedule, Tab. 7 shows that negative values of  $\rho$  consistently enhance performance across tasks, indicating that spending more iterations in the low-noise regime benefits the refinement step. This behavior aligns with our EM-style interpretation: once the diffusion model

$\bar{\sigma}$	SR × 4		Inpainting	Gaussian Blur	Motion Blur	Nonlinear Blur	HDR	NFE
	SSIM $\uparrow$ / LPIPS $\downarrow$ / FID $\downarrow$	SSIM $\uparrow$ / LPIPS $\downarrow$ / FID $\downarrow$	SSIM $\uparrow$ / LPIPS $\downarrow$ / FID $\downarrow$	SSIM $\uparrow$ / LPIPS $\downarrow$ / FID $\downarrow$	SSIM $\uparrow$ / LPIPS $\downarrow$ / FID $\downarrow$	SSIM $\uparrow$ / LPIPS $\downarrow$ / FID $\downarrow$	SSIM $\uparrow$ / LPIPS $\downarrow$ / FID $\downarrow$	SSIM $\uparrow$ / LPIPS $\downarrow$ / FID $\downarrow$
0.2	<b>0.798</b> / 0.182 / 52.2	<b>0.819</b> / <b>0.138</b> / 43.3	<b>0.799</b> / 0.185 / 60.1	<b>0.836</b> / 0.144 / 43.6	<b>0.750</b> / 0.204 / 63.0	<b>0.832</b> / 0.174 / 45.7		74
0.5	<u>0.782</u> / <u>0.176</u> / 48.6	<u>0.814</u> / <b>0.138</b> / <u>41.9</u>	<u>0.783</u> / 0.171 / 51.2	<u>0.828</u> / <u>0.136</u> / 38.7	0.744 / 0.195 / 52.6	<u>0.831</u> / 0.171 / 42.8		100
1.0	0.774 / <b>0.175</b> / <u>46.7</u>	0.811 / <u>0.139</u> / <b>41.8</b>	0.774 / <u>0.168</u> / <u>48.7</u>	0.826 / <b>0.135</b> / <b>37.9</b>	0.744 / 0.193 / <u>51.4</u>	0.831 / <u>0.169</u> / <u>41.4</u>		116
2.0	0.772 / 0.175 / <b>45.6</b>	0.808 / 0.140 / 42.6	0.771 / <b>0.167</b> / <b>47.7</b>	0.826 / 0.135 / 38.0	<u>0.745</u> / <u>0.192</u> / 51.5	0.829 / <b>0.168</b> / <b>40.5</b>		134
5.0	0.771 / 0.176 / 45.6	0.803 / 0.143 / 42.9	0.770 / 0.168 / 47.7	0.826 / 0.135 / 37.9	<u>0.746</u> / <b>0.191</b> / <b>51.3</b>	0.790 / 0.210 / 55.7		152

Table 6. Quantitative comparison for varying  $\bar{\sigma}$  on 100 validation images of **FFHQ**. Metrics are reported as **SSIM $\uparrow$  / LPIPS $\downarrow$  / FID $\downarrow$** . **Bold** indicates the best result; underlined values denote the second best. All measurements include additive Gaussian noise with  $\gamma = 0.05$  and  $\rho = -7$ .

$\rho$	SR × 4		Inpainting	Gaussian Blur	Motion Blur	Nonlinear Blur	HDR	NFE
	SSIM $\uparrow$ / LPIPS $\downarrow$ / FID $\downarrow$	SSIM $\uparrow$ / LPIPS $\downarrow$ / FID $\downarrow$	SSIM $\uparrow$ / LPIPS $\downarrow$ / FID $\downarrow$	SSIM $\uparrow$ / LPIPS $\downarrow$ / FID $\downarrow$	SSIM $\uparrow$ / LPIPS $\downarrow$ / FID $\downarrow$	SSIM $\uparrow$ / LPIPS $\downarrow$ / FID $\downarrow$	SSIM $\uparrow$ / LPIPS $\downarrow$ / FID $\downarrow$	SSIM $\uparrow$ / LPIPS $\downarrow$ / FID $\downarrow$
-2	0.772 / 0.192 / 56.4	<u>0.811</u> / <b>0.141</b> / 44.4	<b>0.790</b> / <b>0.162</b> / <b>46.3</b>	<b>0.840</b> / <b>0.126</b> / <b>32.5</b>	<b>0.751</b> / <b>0.187</b> / <b>51.2</b>	<u>0.833</u> / <u>0.174</u> / 45.9		134
-5	<u>0.780</u> / <u>0.177</u> / <u>47.2</u>	<b>0.812</b> / 0.141 / <u>42.7</u>	<u>0.785</u> / <u>0.169</u> / <u>50.4</u>	<u>0.831</u> / <u>0.134</u> / <u>36.5</u>	<u>0.747</u> / <u>0.192</u> / <u>51.4</u>	<b>0.834</b> / <b>0.169</b> / <b>42.0</b>		107
-7	<b>0.781</b> / <b>0.176</b> / <b>46.0</b>	0.812 / 0.141 / <b>42.1</b>	0.784 / 0.171 / 51.1	0.829 / 0.136 / 37.9	0.744 / 0.195 / 52.6	0.834 / 0.169 / <u>42.3</u>		100
2	0.708 / 0.261 / 80.1	0.793 / 0.170 / 50.5	0.729 / 0.233 / 71.9	0.770 / 0.198 / 60.2	0.680 / 0.275 / 78.6	0.790 / 0.213 / 52.5		56
5	0.772 / 0.196 / 55.0	0.810 / 0.147 / 44.0	0.767 / 0.195 / 58.9	0.807 / 0.159 / 47.9	0.720 / 0.223 / 63.9	0.820 / 0.184 / 46.5		71
7	0.778 / 0.189 / 52.2	<u>0.811</u> / <u>0.145</u> / 44.4	0.772 / 0.190 / 57.4	0.812 / 0.154 / 45.9	0.727 / 0.215 / 62.3	0.823 / 0.182 / 46.2		74

Table 7. Quantitative comparison for varying  $\bar{\rho}$  on 100 validation images of **FFHQ**. Metrics are reported as **SSIM $\uparrow$  / LPIPS $\downarrow$  / FID $\downarrow$** . **Bold** indicates the best result; underlined values denote the second best. All measurements include additive Gaussian noise with  $\gamma = 0.05$  and  $\bar{\sigma} = 0.5$ .

provides a reliable initialization, allocating more resolution to small-noise updates improves measurement consistency without sacrificing stability.

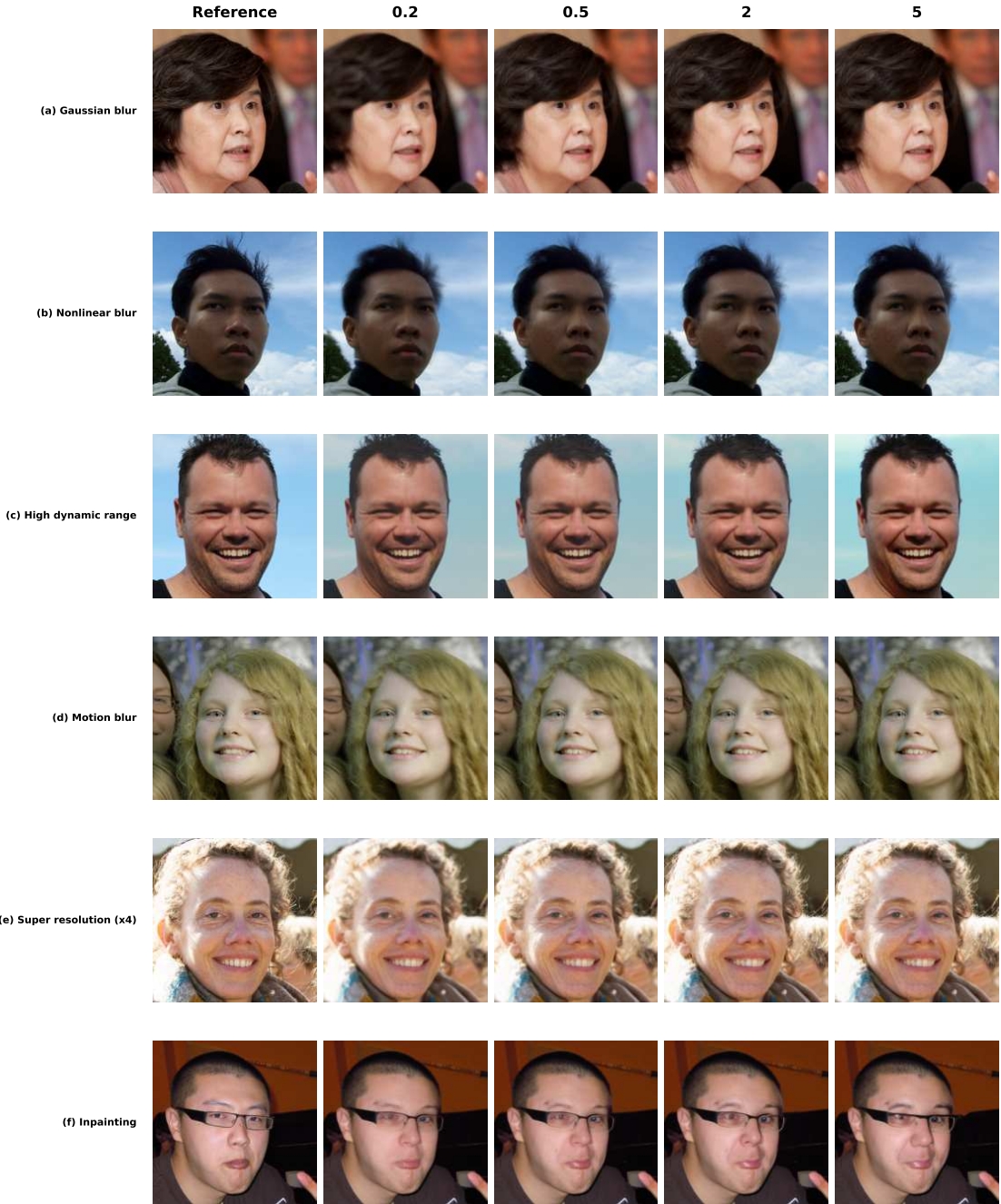


Figure 10. Qualitative results on representative inverse problems on the FFHQ-256 dataset. We compare reconstructions across varying noise refinement threshold  $\bar{\sigma} \in \{0.2, 0.5, 2.0, 5.0\}$ . The tasks are: (a) Gaussian blur reconstruction; (b) Nonlinear blur reconstruction; (c) High dynamic range (HDR) reconstruction; (d) Motion blur reconstruction; (e) 4 $\times$  super-resolution; and (f) Box inpainting.

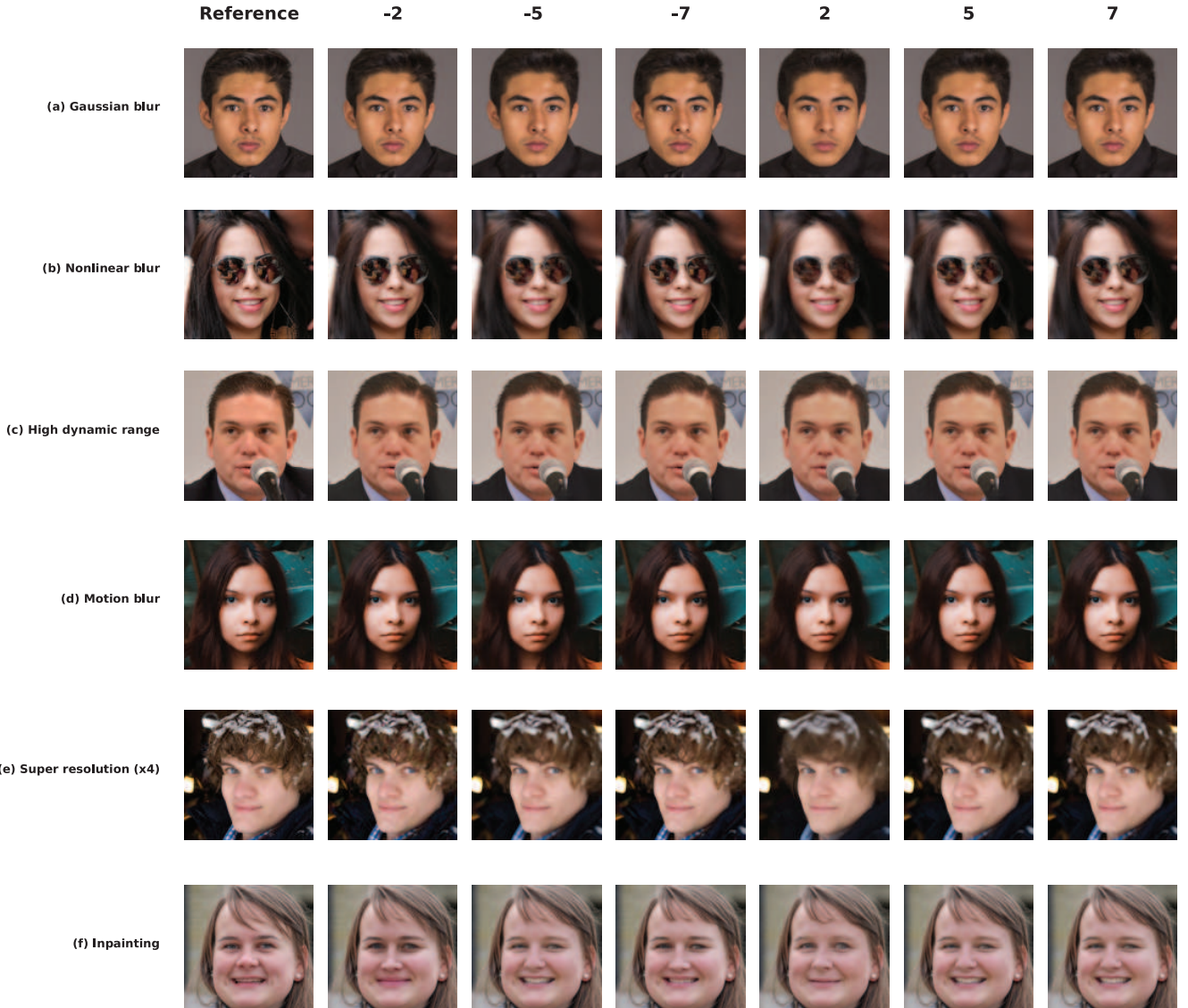


Figure 11. Qualitative results on representative inverse problems on the FFHQ-256 dataset. We compare reconstructions across varying polynomial interpolation schedules  $\rho \in \{-2, -5, -7, 2, 5, 7\}$ . The tasks are: (a) Gaussian blur reconstruction; (b) Nonlinear blur reconstruction; (c) High dynamic range (HDR) reconstruction; (d) Motion blur reconstruction; (e) 4 $\times$  super-resolution; and (f) Box inpainting